IEEE Access
Multidisciplinary : Rapid Review : Open Access Journal

Received May 6, 2020, accepted May 27, 2020, date of publication June 2, 2020, date of current version June 15, 2020.

Digital Object Identifier 10.1109/ACCESS.2020.2999477

A Miniature Piezoresistive Transducer and a New Temperature Compensation Method for New Developed SEM-Based Nanoindentation Instrument Integrated With AFM Function

SEN GU[1], JUNHUI ZHU[2], PENG PAN[3], YONG WANG[2], AND CHANGHAI RU[1,4], (Member, IEEE)
[1]School of Mechanical and Electrical Engineering, Soochow University, Suzhou 21502, China
[2]School of Mechatronic Engineering and Automation, Shanghai University, Shanghai 200072, China
[3]Department of Mechanical Engineering, McGill University, Montreal, QC H3A 0C3, Canada
[4]Research Center of Robotics and Micro Systems and Collaborative Innovation Center of Suzhou Nano Science and Technology, Soochow University, Suzhou 215021, China

Corresponding author: Changhai Ru (rzh@suda.edu.cn)

This work was supported in part by the National Natural Science Foundation of China under Grant 61774107, and in part by the Construction Project of Suzhou Late-Model Research and Development Institutions under Grant SZS2018337.

ABSTRACT Instrumented indentation test inside SEM has become a versatile method for nanomechanical characterization and studying of deformation and failure mechanisms of coating materials at nano-to micro-scale thickness. However, the existing SEM-based nanoindentation instrument cannot acquire surface roughness of coating materials at nano-to micro-scale thickness before nanoindentation and the morphology of residual imprints in real-time inside SEM after nanoindentation. To overcome those two limitations, a new SEM-based nanoindentation instrument integrated with AFM function has been developed. This paper presents a miniature piezoresistive transducer capable of measuring force up to $\pm$2.5N with a resolution of 0.5μN, and measuring displacement up to $\pm$36μm with a resolution of 0.01nm for new developed SEM-based nanoindentation instrument. The transducer design, optimization, readout electronics and characterization are described. Cross-shape compliant mechanism is adopted considering the influence of the lateral force during nanoindentation process. Moreover, four piezoresistive bar-type semiconductor strain gauges (SCSG) have been glued on the cross-shape compliant mechanism enabling the transducer has a compact structure. A new temperature compensation method for SCSG sensors is proposed and solves the problem of amplifier saturation compared with traditional temperature compensation method. Compared with the existing widely used capacitive-based transducer for instrumented indentation test inside SEM, cross-shape piezoresistive transducer shows larger measured ranges. Compared with the existing piezoresistive-based transducer for instrumented indentation test inside SEM, cross-shape piezoresistive transducer shows better resolutions. In the end, the validation test of AFM imaging inside HITACHI SU5000 using standard AFM calibration chip SiC/0.75 is tested.

INDEX TERMS SEM-based instrument indentation test, piezoresistive transducer, temperature compensation, SEM, AFM.

I. INTRODUCTION

Instrumented indentation test inside SEM has become a versatile method for nanomechanical characterization and studying of deformation and failure mechanisms of coating materials at nano- to micro-scale thickness. Knowledge of mechanical properties, deformation mechanism and failure mechanism is of importance for material behavior prediction as well as the development of new materials with desired properties[1]. Tensile testing, bending testing and

The associate editor coordinating the review of this manuscript and approving it for publication was Zheng Chen.

This work is licensed under a Creative Commons Attribution 4.0 License. For more information, see https://creativecommons.org/licenses/by/4.0/

compression testing need tested sample in a standard shape, which limits the possibility to analyze straightforwardly a material on its original shape [2]–[5]. Nanoindentation mechanical testing technique presses a indenter tip with standard geometries, such as Berkovich and Cube Corner, into material surface with controlled force or controlled displacement and then withdraw. The indented displacement and force data are continuously measured, which allows the mechanical properties to be directly extracted from the load-displacement curves based on Oliver-Pharr theory [6]–[7]. Mechanical properties of coating deposited over a surface treatment that changes the original material surfaces properties on nano- to micro-scale depth can be better characterized by instrumented indentation testing method because of its simple preparation and automation [8]–[10]. Moreover, Correlative in-situ analysis with high-resolution SEM, instrumented indentation test can be real-time observation, which allows for visualization and detection of correlation of events that accompany coating deformation (such as cracking, delamination and microstructural changes) with the corresponding features in the force-displacement curve [11], [12].

Many in-situ SEM nanoindentation instruments have been developed [13]–[16], but these share two main common limitations to characterize coating at nano- to micro-scale thickness. The measured mechanical properties of coating at nano- to micro-scale thickness are highly sensitivity to surface roughness [17], [18]. The procedure for extracting mechanical properties from load-displacement curve was developed by Oliver and Pharr and the Oliver-Pharr method requires tested sample with a flat polished defect free surface [18]. However, that requirement has difficulties in obtaining coating at nano- to micro-scale thickness. Moreover, the maximum indentation depth of coating material is 10% of the deposed thickness, which is widely accepted rule-of-thumb to avoid substrate effects in the nanoindentation response. As a consequence, the surface roughness cause a significant error for measuring the practical indentation depth of coating at nano- to micro-scale thickness. Then the analysis of load-displacement curve is highly affected. Other drawback of existing in-situ SEM nanoindentation instruments is unable to acquire the morphology of residual imprints in real-time inside SEM after nanoindentation.

To overcome the two limitations, a new SEM-based nanoindentation instrument integrated with AFM function has been developed, as shown in Fig. 1 (a). It has two sensing device, a transducer for measuring indentation displacement and force during nanoindentation and a self-sensing piezoresistive cantilever (PRC-DF40P, Seiko-Instruments Nanotechnology Inc, stiffness: 40nN/nm, cone angle $< 10°$) for measuring probe-surface contact mechanical force during AFM imaging. The transducer and PRC are attached to Z fine nanopositioner. X-Y fine nanopositioner raster scans the tested sample surface. Both Z fine nanopositioner and X-Y nanopositioner are actuated by piezoelectric ceramics. X-Y stick-slip nanopositioner and Z stick-slip nanopositioner

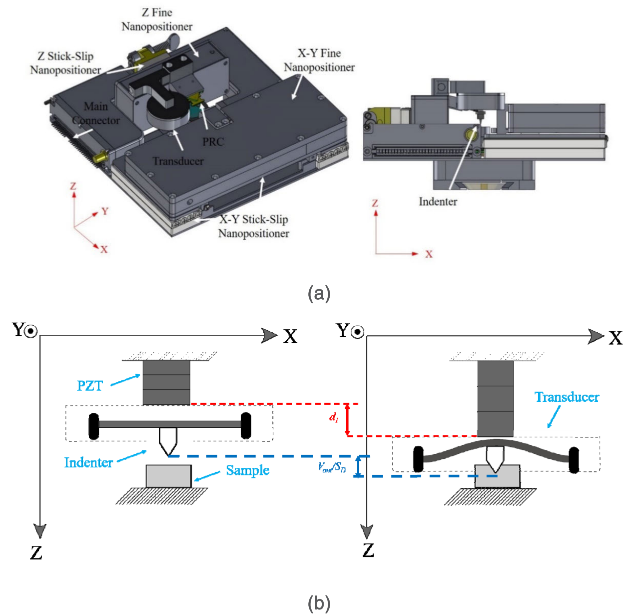

FIGURE 1. (a) In-situ SEM nanoindentation instrument integrated with AFM function; (b) Measuring method for indentation depth and indentation load.

are used to position between indenter tip, PRC and tested sample surface. The new developed instrument is designed to have a compact size of 100mm × 100mm × 32mm, and it is connected to controller that is outside SEM chamber by main connector. As shown in Fig. 1(b), the indentation depth h can be obtain by

$$h = d_1 - \frac{V_{out}}{S_D} \tag{1}$$

where d_1 is the displacement of the Z-PZT actuator that measured by strain gauge sensors in Z nanopositioner. V_{out} and S_D are voltage change during nanoindentation and displacement sensitivity of transducer. The indentation load P applied to the sample surface can be obtained simultaneously as

$$P = \frac{V_{out}}{S_F} \tag{2}$$

where V_{out} and S_F are voltage change during nanoindentation and force sensitivity of transducer. Using the new SEM-based nanoindentation instrument to characterize coating at nano- to micro-scale thickness, the arithmetic roughness (Ra) of interested local surface area is firstly measured by AFM function. Then the minimum indented depth, larger than 20 times of Ra[19], is determined. And, whether the interested local surface area of coating at nano- to micro-scale thickness is able to be tested, can be also determined by comparing the minimum indented depth and the 10% of the deposed thickness. The new developed nanoindentation instrument integrated with AFM function enables to determine the precise indentation depth for characterizing coating at nano- to micro-scale thickness. Moreover, the morphology of residual imprints after instrumented indentation test can be observed by AFM function. Slip steps evolving and discrete events

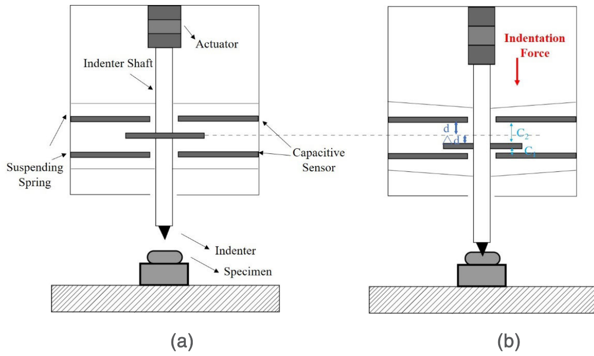

FIGURE 2. The existing transducer with capacitive sensor: (a) initial state; (b) working stage.

during nanoindentation are measured, which is the key understanding the dislocation-based deformation mechanism for coating materials at nano- to micro-scale thickness.

This paper presents the design, optimization and characterization of a miniature piezoresistive transducer that integrated to the new developed SEM-based nanoindentation instrument. The transducer continuously measure the load and displacement data of the indenter tip into the coating surface. Transducer is based on an elastic body whose deformation is measured by sensing devices. Fig. 2 shows the schematic of existing widely used capacitive-based transducer. The transducer measures the force-induced displacement of two parallel suspending springs as a capacity variation of parallel capacitive electrodes. An indentation force applied to suspending springs results in a change of the gaps between the electrodes, which can be measured by a change in capacitance

$$C_1 - C_2 = \varepsilon \cdot A \cdot \left(\frac{1}{d - \Delta d} - \frac{1}{d + \Delta d}\right) \tag{3}$$

where C is the capacitance, ε is the permittivity of environment, d is the initial gap between the capacitor electrodes, Δd is the change of this gap (induced by the applied force) and A is the overlapping area of the capacitor electrodes. The force sensitivity $S_{cap-force}$ and displacement sensitivity $S_{cap-displacement}$ are

$$S_{cap-force} = \frac{\partial V_{out}}{\partial F} = C_{CVC} \cdot \varepsilon \cdot A \cdot k \cdot \left(\frac{2}{d^2 - \Delta d^2}\right) \tag{4}$$

$$S_{cap-displacement} = \frac{\partial V_{out}}{\partial D} = C_{CVC} \cdot \varepsilon \cdot A \cdot \left(\frac{2}{d^2 - \Delta d^2}\right) \tag{5}$$

where C_{CVC} is the constant coefficient of capacitance-to voltage converter, k is the stiffness of the suspending springs. The capacitive-based transducer has the advantage of high sensitivity [20], [21], but it has an inherent non-linearity of force sensitivity and displacement, as shown (4) and (5), which limits its measured force and displacement ranges. Piezoresistive-based transducer measures the force and displacement based on the variation of the specific resistance of a materials induced by applied stress [22], [23]. It allows for the highest level of miniaturization, but is limited to a relatively low sensitivity. The piezoresistive-based transducer that proposed by Rabe [13] has a bad resolution of 4 μN. A new miniature piezoresistive bar-type semiconductor transducer with higher resolution and larger measured ranges is proposed and designed.

Bar-type semiconductor is highly sensitive to temperature change. The SEM vacuum environment has poor heat dissipation, which will result in continuous drift of the force signal and displacement signal during nanoindentation test. *A.L. Window* proposed an operation produce to manually find the proper resistance and the bridge connection of compensation resistors in a 2D space [24]. However, the traditional temperature compensation method will cause the problem of amplifier saturation for the new developed SEM-based nanoindentation instrument integrated with AFM function. To overcome this limitation, a modified temperature compensation method was proposed in this paper.

In the first part, the working principle of transducer is given. This is followed by designing the transducer with high output sensitivity and the readout circuit. Details on how the modified temperature compensation for bar-type SCSG sensors was conducted are presented next. Finally, test results are presented to show the successful development of the Transducer for new developed nanoindentation instrument integrated AFM function.

II. TRANSDUCER DESIGN

A. WORKING PRINCIPLE

This work focuses on piezoresistive bar-type semiconductor strain gauge (SCSG) sensor because of its high sensitivity and ultra-compact size. Fig. 3 shows the transducer and its working principle. It consists of a cross-shape compliant mechanism and four bar-type SCSG glued on the clamped ends of beams. The four beams are the deformation parts. Two bar-type SCSG are glued on upper surfaces subjected to compression stress and the other two bar-type SCSG are glued on bottom surfaces subjected to tension stress. The resistances of four bar-type SCSG make a Wheatstone bridge. An indentation force applied to the middle area results in a relative motion and translates into strain through the cross-shape compliant mechanism, which can be measured by Wheatstone bridge as a change of resistance. The transducer enables to measure positive and negative forces, displacements. And its output V_{out} is proportional to the difference in resistances of four bar-type SCSG.

$$V_{Out} = V_{cc} \times (|k_1 \cdot \varepsilon_1| + |k_2 \cdot \varepsilon_2| + |k_3 \cdot \varepsilon_3| + |k_4 \cdot \varepsilon_4|) \tag{6}$$

where k_1, k_2, k_3 and k_4 are the gauge factors of four bar-type SCSG sensors, and ε_1, ε_2, ε_3, ε_4 are the strain values at four clamped ends of the deformation beams, V_{cc} is reference voltage.

The relationship between load, displacement and output voltage (e.g., sensitivity S_{Force}, S_{Dis}) are given by

$$S_{Force} = \frac{V_{cc} \times (|k_1 \cdot \varepsilon_1| + |k_2 \cdot \varepsilon_2| + |k_3 \cdot \varepsilon_3| + |k_4 \cdot \varepsilon_4|)}{\Delta F} \tag{7}$$

$$S_{Dis} = \frac{V_{cc} \times (|k_1 \cdot \varepsilon_1| + |k_2 \cdot \varepsilon_2| + |k_3 \cdot \varepsilon_3| + |k_4 \cdot \varepsilon_4|)}{\Delta L} \tag{8}$$

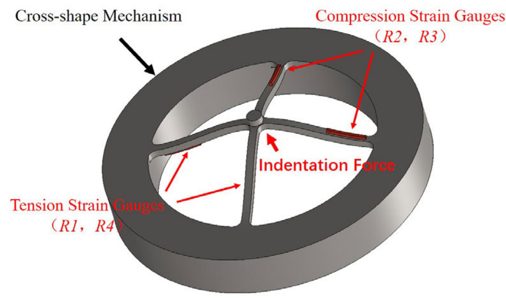

(a)

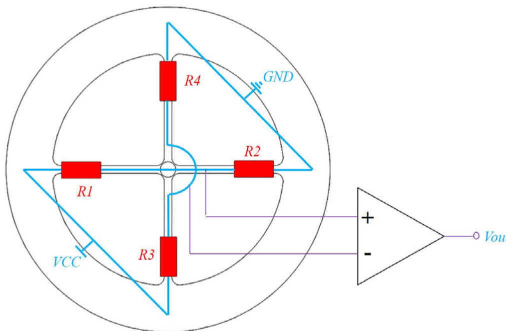

(b)

FIGURE 3. **(a) The cross-shape transducer; (b) The working principle.**

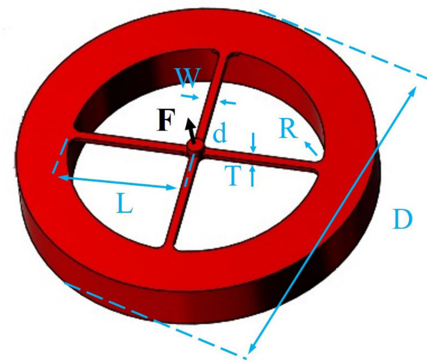

(a)

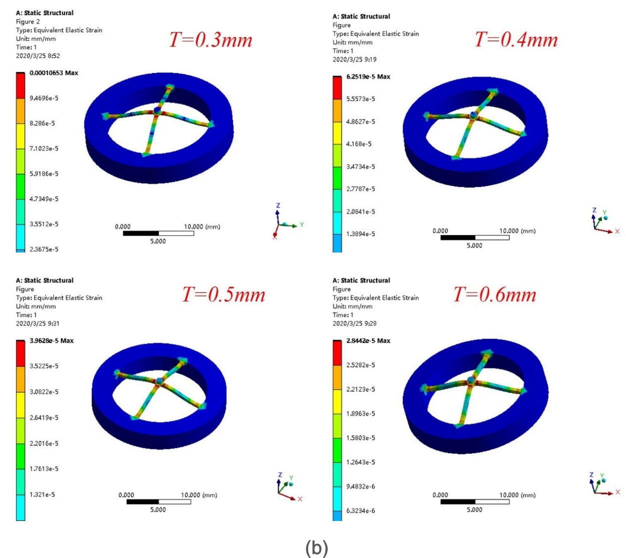

(b)

FIGURE 4. **Cross-shape mechanism: (a) Geometry; (b) The maximum Stress with different beam thickness.**

B. CROSS-SHAPE MECHANISM DESIGN

According to the (7) and (8), both the force and displacement sensitivities of transducer are determined by the strain and gauge factors. Four bar-type SCSG (MICRO INSTRUMENT Company, USA) with high gauge factors have been selected to have highest sensitivity [25]–[28]. Therefore, the cross-shape compliant mechanism should be designed to have large strain values at clamped ends of cross-shape beams.

Considering the influence of the lateral force during nanoindentation process, the cross-shape compliant mechanism is adopted. The Titanium alloy is chosen as the material of cross-shape compliant mechanism with the advantages of good elastic modulus, high strength, SEM vacuum-compatible and machining precision. The diameter of the outer circle is defined as D, and the diameter of the central circle and fillet radius of beam are d and R. The thickness, width and length of the beams are T, W and L, respectively, as shown in Fig. 4 (a).

The cross-shape compliant mechanism can be seen as clamped-clamped beams. The maximum stress σ of every beam can be calculated using the following expression when a normal force F is applied.

$$\sigma = \frac{\frac{3}{4} \times \left(L - \frac{d}{2} - R\right)}{WT^2} F \tag{9}$$

The maximum strain of every beam is given by

$$\varepsilon = \frac{\sigma}{E} = \frac{\frac{3}{4} \times \left(L - \frac{d}{2} - R\right)}{WT^2 \cdot E} F \tag{10}$$

where E is the Young modulus of the cross-shape compliant mechanism. From (10), it can be observed that the strain of beams depends on the material and geometric parameters, and the thickness is the most influence factor. First, the diameter of outer circle (D) is determined as 21 mm, the central circle (d) is 1 mm, and the width (W) and length (L) of beam are 0.5 mm and 7.5 mm, respectively. Then, applying (10), the maximum strain at beam of cross-shape compliant mechanism with different thickness can be calculated.

The finite element simulations have been conducted to calculated the quantitative mechanical response of the transducer to an applied force at its center area. ANSYS workbench software is selected, and the material parameters of Titanium alloy are shown in Table 1. A value 0.1 N of normal force F is applied. Fig. 4 (b) shows the simulated results with different thickness of beam. Table 2 shows the calculated values and simulated values of maximum strain with different thickness. It can be found that the calculated values are close to the simulated values. This indicates the stain at clamped ends of beams can be simulated by finite element method. The strain increases with the decrease of thickness. In the present

TABLE 1. Material parameters of titanium alloy.

Young Modulus (Mpa)	Poisson rate	Tensile Strength (Mpa)	Yield Strength (MPa)
96000	0.36	1070	930

TABLE 2. Maximum strain of cross-shape mechanism with different thickness.

Thickness (mm)	0.3	0.4	0.5	0.6
Simulation	1.0653E-4	6.2519E-5	3.9628E-5	2.8442E-5
Calculation	1.1284E-4	6.3476E-5	4.0625E-5	2.8211E-5
Error (%)	5.5	1.5	2.45	0.8

TABLE 3. Cross-shape mechanism dimensions.

Width (mm) W	0.5
Length (mm) L	7.5
Thickness (mm) T	0.5
Middle circle (mm) d	1
Out circle (mm) D	21
Out circle (mm) R	0.5

study, in order to ensure a larger strain at clamped ends and considering the process difficulty, the thickness of the cross-shape compliant mechanism is selected as 0.5 mm. The dimensions of cross-shape mechanism is listed in Table 3.

C. READOUT CIRCUIT

The SCSG resistance is converted into an analog voltage signal by the Wheatstone bridge, as shown in Fig. 5. The reference voltage *Vcc* of Wheatstone bridge is 5V. Subsequently, the voltage signal is converted into a digital signal using an 24-bit A/D converter (AD7190). The instrument amplifier and RC filter are added between Wheatstone bridge and A/D converter such that the noise level can be highly improved. The converted digital signals A_{out} are received through 32-bit micro-controller STM32F103RCT6. The output voltage V_{out} is given by

$$V_{out} = \frac{5}{2^{24}} \cdot A_{out} \tag{11}$$

III. TEMPERATURE COMPENSATION

A. TEMPERATURE COMPENSATION PRINCIPLE

The aim of temperature compensation for SCSG sensor is to match the apparent thermal coefficient of resistance (TCR) of SCSG by adding fixed resistors, making the differential output of bridge to be zero and common mode voltage output of bridge to be half of *Vcc*, at the maximum and minimum operating temperatures. As shown in Fig. 6, Two fixed resistors (R_{b1}, R_{b2}) are in parallel with and two (R_{c1}, R_{c2}) are in series with two SCSG (R_1, R_3). Due to the TCR of the SCSG sensors, the resistance of the SCSG sensors can be denoted as

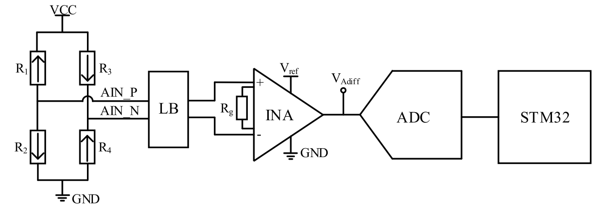

FIGURE 5. Readout circuit design.

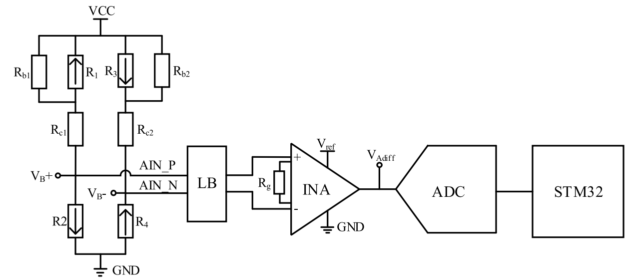

FIGURE 6. Schematic of temperature compensation method.

$$R_i(T) = k_i T + b_i \tag{12}$$

where k_i is the TCR of R_i in the Wheatstone bridge and *bi* is the resistance of *Ri* at T =0°. The compensated $R_{s1}(T_i)$ and $Rs3(T_i)$ are denoted as

$$R_{s1}(T_i) = \frac{R_1(T_i) \times R_{b1}}{R_1(T_i) + R_{b1}} + R_{c1} \tag{13}$$

$$R_{s3}(T_i) = \frac{R_3(T_i) \times R_{b2}}{R_3(T_i) + R_{b2}} + R_{c2} \tag{14}$$

the compensated differential output voltage $V_{B-diff}(T_i)$ and the compensated common mode output voltage $V_{B-cm}(T_i)$ of the Wheatstone bridge are given by

$$\begin{cases} V_{B-diff}(T_i) = V_{cc}\left[\frac{R_4(T_i)}{R_4(T_i)+R_{s3}(T_i)} - \frac{R_2(T_i)}{R_2(T_i)+R_{s1}(T_i)}\right] \\ V_{B-cm}(T_i) = \frac{V_{cc}}{2}\left[\frac{R_4(T_i)}{R_4(T_i)+R_{s3}(T_i)} + \frac{R_2(T_i)}{R_2(T_i)+R_{s1}(T_i)}\right] \end{cases} \tag{15}$$

$$\begin{cases} V_{B-diff}(T_0) = 0 \\ V_{B-diff}(T_1) = 0 \\ V_{B-cm}(T_0) = \frac{1}{2}V_{cc} \\ V_{B-cm}(T_1) = \frac{1}{2}V_{cc} \end{cases} \tag{16}$$

Assume the bridge is compensated among the temperature range from T_0 to T_1, $V_{B-diff}(T)$ should have zero output and $V_{B-cm}(T)$ is forced to be 0.5Vcc at both T = T_0 and T = T_1. There are totally 16 possible configures by solving the (11), Fig. 6 is one example. However, only one solution yields non-negative resistance values, which are desired compensation resistors.

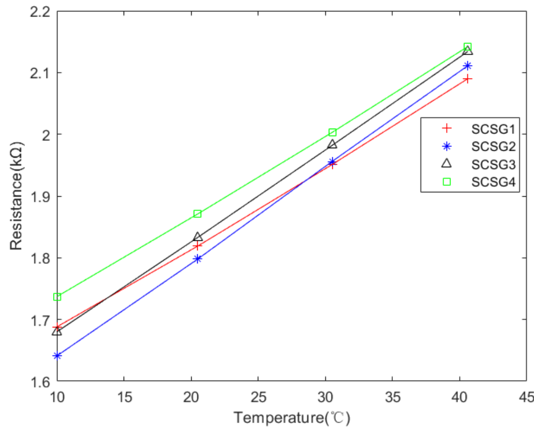

FIGURE 7. Calibration of temperature coefficients for SCSG sensors.

TABLE 4. Primary coefficients of each SCSG.

SCSG	SCSG1	SCSG2	SCSG3	SCSG4
ki	0.01314	0.0154	0.01484	0.01323
bi	1.553	1.485	1.53	1.602

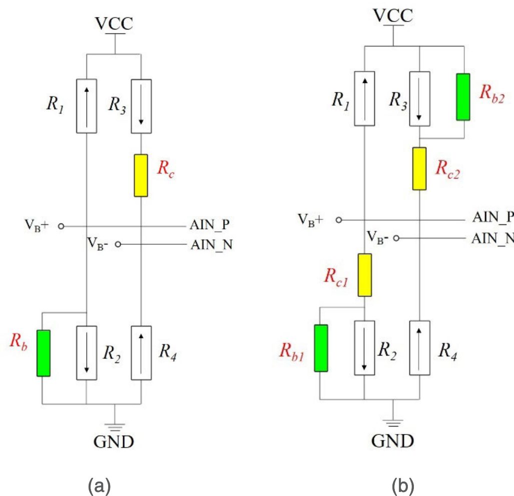

FIGURE 8. Temperature compensation solutions: (a) Traditional method; (b) Modified method in this paper.

B. TEMPERATURE COMPENSATION TEST

The temperature coefficients k_i and b_i of SCSG sensors are calibrated first. The transducer was placed in a temperature chamber. Changing the temperature from 10 ° to 40 ° with a step of 10 ° and recording the resistances of the four SCSG sensors. All the data were fitted into a first-order polynomial in (12) by using the least squares method, the results is shown in Fig. 7. The calibrated k_i and b_i are listed in Table 4.

After calibration of temperature coefficients of the four SCSG sensors, temperature compensation resistances were calculated by solving the (16). The working temperature of our SEM (HITACHI SU5000) chamber is about 30.3°,and the maximum temperature is 45°. Thus, $T_0 = 0°$ and $T_1 = 45°$ are set. Table 5 lists the resistances of four SCSG sensors at 0° and 45°. Using the data of Table 5, there are totally 16 possible solution configurations by solving the (16). Only one set of resistance values for R_{b1}, R_{b2}, R_{c1}, R_{c2} satisfied the non-negative condition. The detailed resistance values for solutions are listed in Table 6 and Fig. 8(b) is the solution.

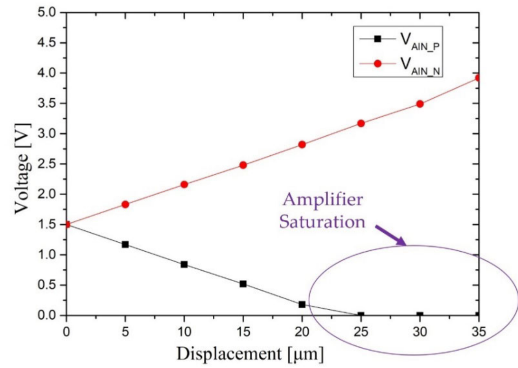

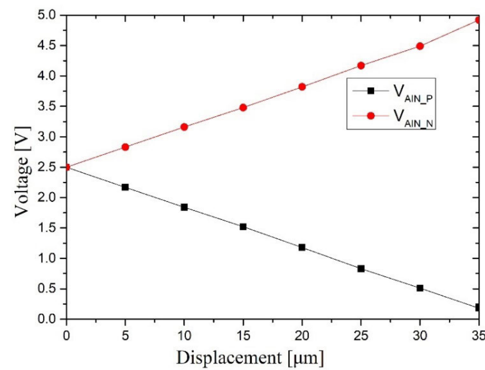

FIGURE 9. Captured on the pins VAIN_P and VAIN_N at the output of the amplifiers: (a) Traditional method; (b) Proposed method in this paper.

Using the setup of Fig. 10 (b), the displacement was increased from 0μm to 35 μm with a step of 5 μm. The output voltages V_{AIN_P} and V_{AIN_N} were measured using a source meter at the Wheatstone bridge. Fig. 9 shows the output voltage results of traditional temperature compensation method (Fig. 8 (a)) and proposed temperature compensation method in this paper. In the traditional method, the amplifier saturation occurred, which cause the usable measurement range of the transducer. Compared with the traditional method, the proposed method in this paper shows better measured range because of the common mode voltage output of the Wheatstone bridge is centered.

IV. CALIBRATION AND CHARACTERIZATION

Combing the (7), (8) and (10), the force sensitivity and displacement sensitivity are given

$$S_{Force} = \frac{\Delta V_{Out}}{\Delta F} = V_E \times (k_1 + k_2 + k_3 + k_4) \times \frac{\frac{3}{4} \times \left(L - \frac{d}{2} - R\right)}{WT^2 \cdot E} \quad (17)$$

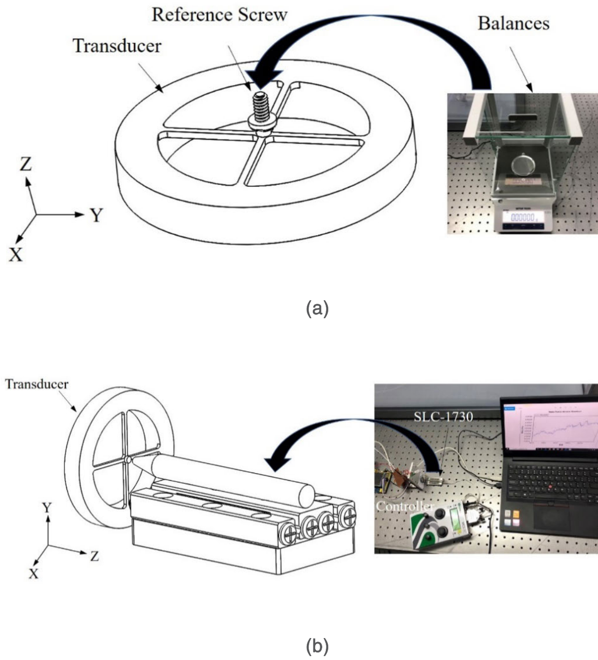

FIGURE 10. Transducer calibration: (a) Schematic of force characterization; (b) Schematic of displacement characterization.

TABLE 5. The corresponding resistance values of each scsg at 0 ° and 45 0 °.

Temperature ℃	SCSG1 R_1/ KΩ	SCSG2 R_2/ kΩ	SCSG3 R_3/ kΩ	SCSG4 R_4/ kΩ
0	1.553	1.485	1.53	1.602
45	1.553	1.485	1.53	1.602

TABLE 6. Compensation resistance values.

R_{c1} KΩ	R_{c2} kΩ	R_{b1} kΩ	R_{b2} kΩ
0.4757	0.1271	10.0086	10.0086

$$S_{Displacement} = \frac{\Delta V_{Out}}{\Delta L} = V_E \times (k_1 + k_2 + k_3 + k_4) \times \frac{\frac{3}{4} \times \left(L - \frac{d}{2} - R\right)}{WT^2 \cdot E} \times K \tag{18}$$

where K is the stiffness of cross-shape compliant mechanism. According to [29], the stiffness K can be calculated by

$$K = \frac{4EWT^3}{\left(L - \frac{d}{2} - R\right)^3} \tag{19}$$

Equation (18) can be further described by

$$S_{Displacement} = \frac{\Delta V_{Out}}{\Delta L} = V_E \times (k_1 + k_2 + k_3 + k_4) \times \frac{3T}{\left(L - \frac{d}{2} - R\right)^2} \tag{20}$$

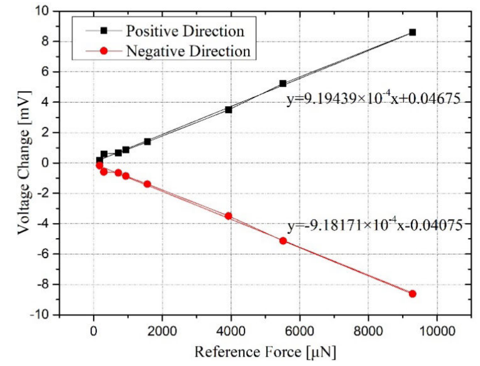

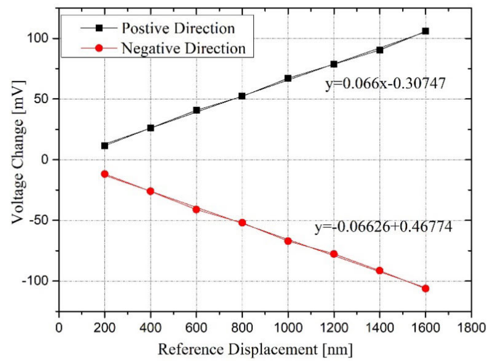

FIGURE 11. Transducer sensitivity: (a) Output voltages for the loads; (b) Output voltages for the displacements.

Precise calibration of transducer is difficult for reasons, including the need to apply SI traceable reference force and known displacement at precise positions. The goal of the transducer is to obtain the calibration value, which describe the linear relationship between the output voltage V_F,, V_D of the transducer and the applied force F and displacement D :

$$F = V_F \cdot S_F \tag{21}$$

$$D = V_D \cdot S_D \tag{22}$$

For the force calibration of the cross-shape transducer, eight screws with reference forces are used. The eight screws are measured by a balances (METTLER TOLEDO Company, Switzerland), and then placed on the central circle, as shown in Fig. 10 (a). Using the least-squares method to fit the raw data, the best estimate of the calibration values are found. From the Fig. 11(a), the force sensitivities S_F at positive and negative directions are 9.19439×10^{-4}mV/μN and -9.18171×10^{-4}mV/μN, respectively. Solving the fitting equation at the maximum voltage change of ±2.5 V, the force range of transducer is ±2.5 N.

For the displacement calibration of cross-shape transducer, eight known displacement are used. The eight displacement were provide by piezoelectric drive stick-slip drive nanopositioner (SLC-1730, SMARACT Company, German) at closed-loop control, as shown in Fig. 10 (b). Using the least-squares method to fit the raw data, the best estimate

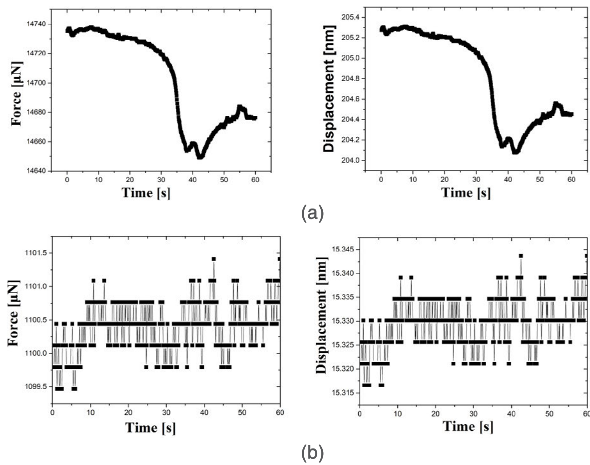

FIGURE 12. Transducer resolution: (a) Without proposed temperature compensation method; (b) Using the proposed temperature compensation method.

TABLE 7. Transducer characteristics.

	This paper	Piezoresistive sensor[13]	Capacitive sensor[16]
Force resolution	0.5 μN	4 μN	0.5 μN
Force range	±2.5 N	±500 mN	±10 mN
Displacement resolution	0.01 nm	1 nm	1 nm
Displacement range	±36 μm	±40 μm	±5 μm

of the calibration values are found. From the Fig. 11 (b), the displacement sensitivities S_D at positive and negative directions are 0.066 mV/nm and −0.06626 mV/nm, respectively. Solving the fitting equation at the maximum voltage change of ±2.5 V, the force range of transducer is ±36 μm.

The resolution is the smallest force increment that can be detected, limited by the noise in the transducer output. The noise is the change in the transducer output signal without any changes of the applied force. We follow ISO 5725 Standard on Accuracy (trueness and precision of measurement methods and results) that defines precision as the standard deviation (RMS value) of the measurement data[20]. The standard deviation of the noise level of the piezoresistive transducer with and without proposed temperature compensation correspond to 0.5 μN, 0.01 nm and 31 μN, 0.4 nm respectively, at a readout frequency of 10Hz, as shown in Fig. 12.

Table 7 lists the main parameters of transducer and other widely used transducer. Compared with existing capacitive-based transducer, our proposed transducer has larger measured ranges. Compared with existing piezoresistive-based transducer, our proposed transducer has better measured resolution.

(a)

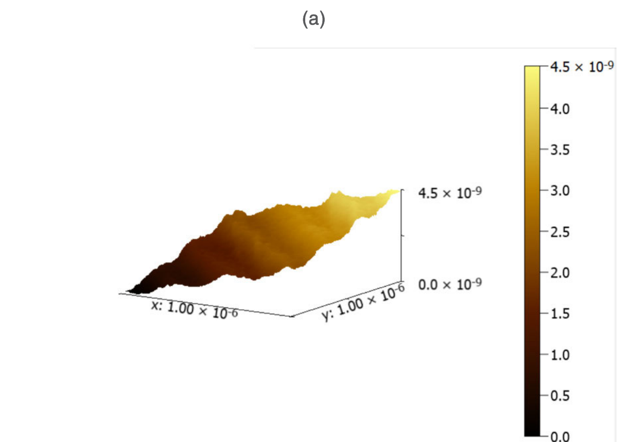

(b)

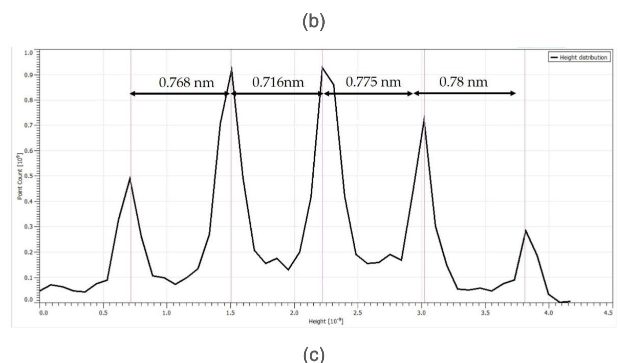

(c)

FIGURE 13. Validation for the new developed nanoindentation instrument integrated AFM function using the standard chip SiC/0.75. (a) Testing inside HITACHI SU 5000; (b) The 3D view of the sample topography; (c) The height spectrum analysis of the sample topography.

V. VALIDATION OF AFM IMAGING USING SiC/0.75

The advantage of new developed nanoindentation instrument is the integrated AFM function. In order to validate the resolution of the AFM imaging working inside HITACHI SU5000, a standard AFM calibration chip SiC/0.75 from NT-MDT was used. The chip contains a piece of 6H-SiC crystal, which was etched by HCI to generate 6H-SiC [0001] surface with uniform half-monolayer steps of the C-face. The steps on the chip were not visible using the SEM imaging, as shown in Fig. 13 (a), but AFM can clearly reveal the steps, as shown in Fig. 13 (b). From the height spectrum analysis

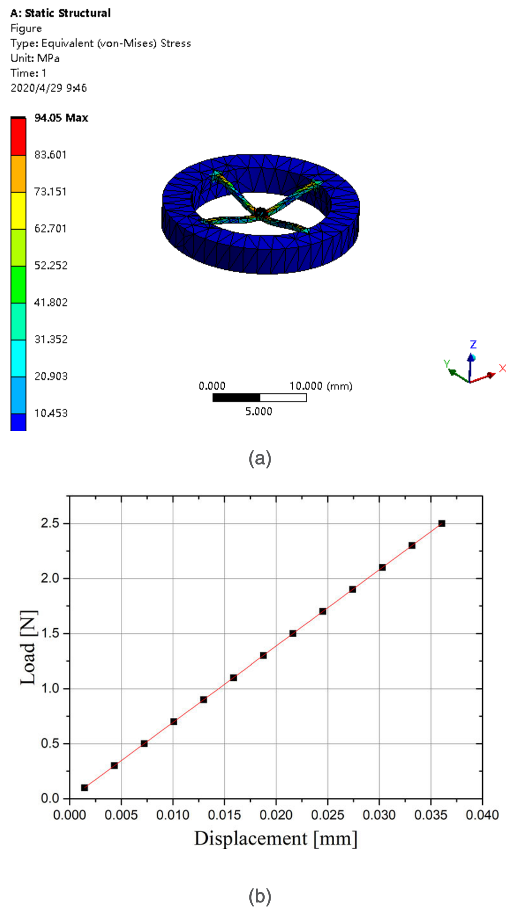

FIGURE 14. (a) FE simulation result of the maximum stress under maximum load of 2.5 N; (b) the relationship between the applied load and the deflection of the cross-shape mechanism.

in Fig. 13 (c), the average height distance between adjacent peaks was measured to be 0.75 nm (N = 4), which matched with the measured result in [30]. The capability of measuring a step height of 7.5 nm for SiC/0.75 was verified in the new developed nanoindentation instrument integrated with AFM function.

VI. DISCUSSION

Equation (9), (10) and (19) are only valid for small deflection, which is generally defined as the regime of beam deflection/length $< 5\%$. Moreover, the linearity of the clamped-clamped beam is also be related to beam thickness. The maximum deflection should be less than a quarter of the beam thickness[5]. The beam deflection/length of cross-shape mechanism equals to 0.5%. The maximum deflection of 36 μm is far less quarter of beam thickness, i.e. 125 μm. When a maximum load of 2.5 N is applied to cross-shape mechanism, the maximum generated stress is 94.05 MPa, as shown in Fig. 14 (a), which is far less than yield strength of Titanium alloy.

Fig. 14 (b) shows the relationship between the vertical deflection of the centre of the cross-shape mechanism and the normal load. it can be observed that the deflection increase linearly with the increasing of the normal load. This indicates that the stiffness of cross-shape mechanism is changeless in the measured ranges.

VII. CONCLUSION

A piezoresistive transducer used for new developed SEM-based nanoindentation instrument integrated with AFM function, its design, optimization and characterization have been presented. Considering the lateral force, the cross-shape compliant mechanism is adopted. And a new temperature compensation method for SCSG sensors is proposed and tested to compared with traditional temperature compensation method. The designed transducer enables force measurements in a range between ± 2.5 N with a resolution down to 0.5 μN and displacement in range between ± 36 μm with a resolution down to 0.01 nm. The main contributions of this work are as follows.

- The compact structure enabling the transducer to be integrated to the new developed SEM-based nanoindentation instrument integrated with AFM function.
- The temperature compensation method for bar-type SCSG sensor, enabling the force resolution and displacement resolution down to 0.5 μN and 0.01 nm.
- The temperature compensation method for bar-type SCSG sensor, enabling the transducer a better measured ranges compared traditional temperature compensation method.
- The transducer has larger measured ranges compare with the existing widely used capacitive-based transducer for instrumented indentation test inside SEM and has better resolutions compared with the existing piezoresistive-based transducer for instrumented indentation test inside SEM.

REFERENCES

[1] F. Rahman, G. Ngaile, and T. Hassan, "Development of scanning electron microscope-compatible multiaxial miniature testing system," *Meas. Sci. Technol.*, vol. 30, no. 10, pp. 1–17, Aug. 2019.

[2] M. Kiuchi, Y. Isono, S. Sugiyama, T. Morita, and S. Matsui, "Mechanical and electrical properties evaluation of carbon nanowire using electrostatic actuated nano tensile testing devices (EANAT)," presented at the 5th IEEE Conf. Nanotechnol., Jul. 2005. [Online]. Available: https://ieeexplore.ieee.org/abstract/document/1500806/

[3] C. Chen, S. Nagao, T. Sugahara, H. Zhang, J. Jiu, K. Suganuma, T. Iwashige, K. Sugiura, and K. Tsuruta, "Effect of size and shape of Ag particles for mechanical properties of sintered Ag joints evaluated by micro-compression test," presented at the Int. Conf. Electron. Packag. (ICEP), Apr. 2017. [Online]. Available: https://ieeexplore.ieee.org/abstract/document/7939340/

[4] T. Tsuchiya, T. Hemmi, J.-Y. Suzuki, Y. Hirai, and O. Tabata, "Tensile strength of silicon nanowires batch-fabricated into electrostatic MEMS testing device," *Appl. Sci.*, vol. 8, no. 6, pp. 1–11, Jun. 2018.

[5] D. Zhang, "A nano-tensile testing system for studying nanostructure inside an electron microscope: Design, characterization and application," Ph.D. dissertation, Swiss Federal Lab. Mater. Test. Res., Dübendorf, Switzerland, 2010.

[6] D. M. Frazer, "Elevated temperature small scale mechanical testing of uranium dioxide," Ph.D. dissertation, Dept. Eng.-Nucl. Eng., Univ. California, Berkeley, Berkeley, CA, USA, 2018.

[7] J. M. Wheeler, "Nanoindentation under dynamic conditions," Ph.D. dissertation, Dept. Mater. Sci. Metall., Univ. Cambridge, Cambridge, U.K., 2009.

[8] S. Papaleo, W. H. Zisser, A. P. Singulani, H. Ceric, and S. Selberherr, ''Stress evolution during nanoindentation in open TSVs,'' *IEEE Trans. Device Mater. Rel.*, vol. 16, no. 4, pp. 470–474, Dec. 2016.

[9] C. Wu, R. Huang, and K. M. Liechti, ''Characterizing interfacial sliding of through-silicon-via by nano-indentation,'' *IEEE Trans. Device Mater. Rel.*, vol. 17, no. 2, pp. 355–363, Jun. 2017.

[10] H. Attar, S. Ehtemam-Haghighi, D. Kent, I. V. Okulov, H. Wendrock, M. Bönisch, A. S. Volegov, M. Calin, J. Eckert, and M. S. Dargusch, ''Nanoindentation and wear properties of Ti and Ti-TiB composite materials produced by selective laser melting,'' *Mater. Sci. Eng., A*, vol. 688, pp. 20–26, Mar. 2017.

[11] I. Lujan-Regalado, A. Kirubanandham, J. J. Williams, and N. Chawla, ''Nucleation and growth of tin hillocks by *in situ* nanoindentation,'' *J. Electron. Mater.*, vol. 48, no. 1, pp. 58–71, Jan. 2019.

[12] Q. Wang, F. Zhou, M. Callisti, T. Polcar, J. Kong, and J. Yan, ''Study on the crack resistance of CrBN composite coatings via nano-indentation and scratch tests,'' *J. Alloys Compounds*, vol. 708, pp. 1103–1109, Jun. 2017.

[13] R. Rabe, ''Compact test platform for *in-situ* indentation and scratching inside a scanning electron microscope (SEM),'' Ph.D. dissertation, EPFL, Lausanne, Switzerland, 2006.

[14] B. Zhang, Y. Song, G. Z. Voyiadjis, and W. J. Meng, ''Assessing texture development and mechanical response in microscale reverse extrusion of copper,'' *J. Mater. Res.*, vol. 33, no. 8, pp. 978–988, Apr. 2018.

[15] X. F. Wang, R. Han, T. L. Han, N. X. Han, and F. Xing, ''Determination of elastic properties of urea-formaldehyde microcapsules through nanoindentation based on the contact model and the shell deformation theory,'' *Mater. Chem. Phys.*, vol. 215, pp. 346–354, Aug. 2018.

[16] E. D. Hintsala, S. Bhowmick, X. Yueyue, R. Ballarini, S. A. S. Asif, and W. W. Gerberich, ''Temperature dependent fracture initiation in microscale silicon,'' *Scripta Mater.*, vol. 130, pp. 78–82, Mar. 2017.

[17] L. Chen, A. Ahadi, J. Zhou, and J.-E. Ståhl, ''Quantitative study of roughness effect in nanoindentation on AISI316L based on simulation and experiment,'' *Proc. Inst. Mech. Eng., C, J. Mech. Eng. Sci.*, vol. 231, no. 21, pp. 4067–4075, Nov. 2017.

[18] H. Liu and J. W. McBride, ''A finite-element-based contact resistance model for rough surfaces: Applied to a bilayered Au/MWCNT composite,'' *IEEE Trans. Compon., Packag., Manuf. Technol.*, vol. 8, no. 6, pp. 919–926, Jun. 2018.

[19] L. Chen, A. Ahadi, J. Zhou, and J.-E. Ståhl, ''Modeling effect of surface roughness on nanoindentation tests,'' *Procedia CIRP*, vol. 8, pp. 334–339, Jan. 2013.

[20] S. D. Muntwyler, ''Microforce-sensing probes and methodologies for micromechanical and dimensional metrology,'' Ph.D. dissertation, ETH Zürich, Zürich, Switzerland, 2010.

[21] Y. Zhang, Y. Oh, D. Stauffer, and A. A. Polycarpou, ''A microelectromechanical systems (MEMS) force-displacement transducer for sub-5 nm nanoindentation and adhesion measurements,'' *Rev. Sci. Instrum.*, vol. 89, no. 4, pp. 105–120, Apr. 2018.

[22] Y. Wei and Q. Xu, ''An overview of micro-force sensing techniques,'' *Sens. Actuators A, Phys.*, vol. 234, no. 18, pp. 359–376, Jan. 2015.

[23] G. Hamdana, M. Bertke, L. Doering, T. Frank, U. Brand, H. S. Wasisto, and E. Peiner, ''Transferable micromachined piezoresistive force sensor with integrated double-meander-spring system,'' *J. Sensors Sensor Syst.*, vol. 6, no. 1, pp. 121–133, Mar. 2017.

[24] A. L. Window, *Strain Gauge Technology*. New York, NY, USA: Elsevier Applied Science, 1992.

[25] N. Kashiri, J. Malzahn, and N. G. Tsagarakis, ''On the sensor design of torque controlled actuators: A comparison study of strain gauge and encoder-based principles,'' *IEEE Robot. Autom. Lett.*, vol. 2, no. 2, pp. 1186–1194, Apr. 2017.

[26] E. DiGiampaolo, A. DiCarlofelice, and A. Gregori, ''An RFID-enabled wireless strain gauge sensor for static and dynamic structural monitoring,'' *IEEE Sensors J.*, vol. 17, no. 2, pp. 286–294, Jan. 2017.

[27] A. Shaker, A. H. Hassanin, N. M. Shaalan, M. A. Hassan, and A. A. El-Moneim, ''Micropatterned flexible strain gauge sensor based on wet electrospun polyurethane/PEDOT: PSS nanofibers,'' *Smart Mater. Struct.*, vol. 28, no. 7, pp. 82–90, Jun. 2019.

[28] Y. Zhao, Y. Zhao, C. Wang, S. Liang, R. Cheng, Y. Qin, P. Wang, Y. Li, X. Li, and T. Hu, ''Design and development of a cutting force sensor based on semi-conductive strain gauge,'' *Sens. Actuators A, Phys.*, vol. 237, pp. 119–127, Jan. 2016.

[29] B. Zhong, ''Research on key technologies of cross-scale precision movement stage based on stick-slip driving,'' Ph.D. dissertation, Harbin Inst. Technol., Harbin, China, 2012.

[30] S. Nie, C. D. Lee, R. M. Feenstra, Y. Ke, R. P. Devaty, W. J. Choyke, C. K. Inoki, T. S. Kuan, and G. Gu, ''Step formation on hydrogen-etched 6H-SiC{0001} surfaces,'' *Surf. Sci.*, vol. 602, no. 17, pp. 2936–2942, Sep. 2008.

SEN GU received the master's degree from the China Academy of Machinery Science and Technology, Harbin Welding Institute, in 2014. He is currently pursuing the Ph.D. degree with the School of Mechanical and Electric Engineering, Soochow University, China. His research interests including stick-slip drive nanopositioner, nanoindentation instrument inside SEM, and AFM inside SEM.

JUNHUI ZHU received the master's degree in mechanical engineering from Soochow University, Suzhou, China. in 2015. He is currently pursuing the Ph.D. degree from the Mechanical and Automation Engineering Department, Shanghai University, Shanghai, China. His research interests including design and fabrication micro-nano electromechanical systems and long-stroke cross-scale nano-positioning technology.

PENG PAN received the master's degree in mechanical engineering from Soochow university, Suzhou, China, in 2016. He is currently pursuing the Ph.D. degree with the Department of Mechanical engineering, McGill University, Montreal, QC, Canada. His research interests include automated robotic manipulation, design, and fabrication of micro-nano electromechanical systems.

YONG WANG received the master's degree in mechanical engineering from Soochow University, Suzhou, China, in 2014. He is currently pursuing the Ph.D. degree with the Mechanical and Automation Engineering Department, Shanghai University, Shanghai, China. His research interests include design and fabrication of miacro-nano electromechanical systems and cross-scale nano-positioning technology.

CHANGHAI RU (Member, IEEE) received the Ph.D. degree in mechatronics engineering from the Harbin Institute of Technology, Harbin, China, in 2005.

He was a Postdoctoral Fellow with the Department of Mechanical and Industrial Engineering, University of Toronto, Toronto, ON, Canada. He is currently a Professor with the Research Center of Robotics and Micro Systems and Collaborative Innovation Center of Suzhou Nano Science and Technology, Soochow University, and the College of Automation, Harbin Engineering University, China. His research interests include micro/nanomanipulation, nanopositioning technologies, and solid-state actuators' driving and control method.